Ferrostatin-1 alleviates oxalate-induced renal tubular epithelial cell injury, fibrosis and calcium oxalate stone formation by inhibiting ferroptosis

JINNA XIE*, ZEHUA YE*, LEI LI, YUQI XIA, RUN YUAN, YUAN RUAN* and XIANGJUN ZHOU*

Department of Urology, Renmin Hospital of Wuhan University, Wuhan, Hubei 430060, P.R. China

Received February 4, 2022; Accepted May 19, 2022

DOI: 10.3892/mmr.2022.12772

Abstract. The present study aimed to evaluate the role and mechanism of ferrostatin-1 (Fer-1) in oxalate (Ox)-induced renal tubular epithelial cell injury, fibrosis, and calcium oxalate (CaOx) stone formation. A CaOx model in mice kidneys was established via intraperitoneal injection of 80 mg/kg glyoxylic acid for 14 days. The mice were randomly divided into three groups (n=6), namely, the control (Con), the CaOx group, and the CaOx + Fer-1 group. Cultured human renal tubular epithelial cells (HK-2 cells) were randomly divided into three groups (n=3), namely, the control (Con), the Ox group, and the Ox + Fer-1 group. The levels of heme oxygenase 1 (HO-1), superoxide dismutase 2 (SOD2), glutathione peroxidase 4 (GPX4), and solute carrier family 7 member 11 (SLC7A11) were assessed by immunofluorescence and western blot analysis. Renal tubular injury and apoptosis were evaluated by H&E and TUNEL staining. Kidney interstitial fibrosis was evaluated by Masson and Sirius red staining, and the levels of E-cadherin, vimentin and α-SMA were detected by immunofluorescence or western blot analysis. Mitochondrial structure was observed using a transmission electron microscope. The levels of reactive oxygen species (ROS) were determined by flow cytometry and CaOx stone formation was evaluated by von Kossa staining. The results revealed that in comparison with the Con group, mitochondrial injury under glyoxylic acid treatment was observed by TEM. The expression of GPX4 and SLC7A11 in the CaOx and Ox groups was downregulated (P<0.05), whereas the expression of HO-1 and SOD2 was upregulated (P<0.05). Renal tissue damage, apoptosis of renal tubular epithelial cells, and interstitial fibrosis were increased in the CaOx and Ox groups (P<0.05). In comparison with the CaOx or Ox group, the expression of GPX4 and SLC7A11 in the CaOx + Fer-1 or Ox + Fer-1 group was upregulated (P<0.05), whereas that of HO-1 and SOD2 was downregulated (P<0.05). Renal tissue damage, apoptosis of renal tubular epithelial cells and interstitial fibrosis were decreased following Fer-1 treatment (P<0.05). The ROS level was also decreased following Fer-1 treatment. Moreover, CaOx stone formation was decreased in the CaOx + Fer-1 group (P<0.05). In conclusion, Fer-1 alleviated Ox-induced renal tubular epithelial cell injury, fibrosis, and CaOx stone formation by inhibiting ferroptosis.

Correspondence to: Dr Xiangjun Zhou, Department of Urology, Renmin Hospital of Wuhan University, 238 Jiefang Road, Wuhan, Hubei 430060, P.R. China
E-mail: zxj19840902@163.com

*Contributed equally

Key words: calcium oxalate stone, ferroptosis, ferrostatin-1, renal tubular epithelial cell, chronic kidney disease

Introduction

Kidney stones are one of the most common urinary diseases in the world, causing heavy social and economic burden to mankind (1). The occurrence and development of kidney stones are closely related to the increased risk of chronic kidney disease (CKD) (2). calcium oxalate (CaOx) stones account for 70-80% of renal stones, 35% of patients with CaOx stones were accompanied by renal injury, and 29% were accompanied by CKD (3). The prevention and treatment of CaOx stones focuses on the causes of CaOx stones and surgical improvement. The treatment of patients with CaOx stones progressing to CKD has not attracted enough attention. Renal injury induced by CaOx crystals cannot be completely repaired and progresses to fibrosis (4). Therefore, the mechanism of fibrosis after CaOx crystal renal injury should be urgently clarified, and the progression of patients with CaOx stones to CKD should be delayed.

The formation process of CaOx stones includes the precipitation of CaOx crystals when oxalate (Ox) and calcium (Ca) ions are in a relatively supersaturated state. CaOx crystals adhere to tubular epithelial cells and interact with other cells. The crystals stay in the kidney in various ways and finally form kidney stones (5). The adhesion of CaOx crystals to renal tubular epithelial cells is the initial process of stone formation. CaOx crystals can directly produce cytotoxic damage (6). Renal tubular epithelial cells undergo apoptosis after injury, resulting in inflammatory response and a fibrotic environment (7). The molecular mechanism in which CaOx crystals induce renal tubular epithelial cell injury and interstitial fibrosis should be explored for the clinical prevention

and treatment of CaOx stone formation and the progression of patients with CaOx stones to CKD.

Ferroptosis is characterized by intracellular iron accumulation and lipid peroxidation during cell death. Ferroptosis can be induced by the downregulation of system XCT activity, inhibition of glutathione peroxidase 4 (GPX4), and increase of reactive oxygen species (ROS) (8). System XCT is an important intracellular antioxidant system, which takes up cystine and excretes glutamate. Inhibiting the activity of system XCT affects the synthesis of glutathione (GSH) by inhibiting the absorption of cystine, which leads to the occurrence of oxidative damage and ferroptosis. Solute carrier family 7 member 11 (SLC7A11) and GPX4 are the central regulators of ferroptosis, and the reduced levels of GPX4 and SLC7A11 are always regarded as markers of ferroptosis. Ferroptosis is involved in tumor development (9), neurodegenerative diseases (10), ischemia-reperfusion injury (11), and other pathological processes, and the targeted regulation of ferroptosis and its signaling pathways have achieved beneficial results. Although the interactions between ferroptosis and acute kidney injury (AKI) have been continuously explored (12), limited studies have focused on ferroptosis and CKD, especially the progression of patients with CaOx stones to CKD. By high-throughput screening of small molecule libraries, studies have independently reported that ferrostatin-1 (Fer-1) acts as a potent inhibitor of ferroptosis (13,14). In the present study, the role and mechanism of Fer-1 in Ox-induced renal tubular epithelial cell injury, fibrosis, and CaOx stone formation were evaluated.

Materials and methods

Animals. A total of 18 C57BL/6J mice (male; 6-8 weeks; weighing 24-28 g) were purchased from Hubei Provincial Centers for Disease Control and Prevention. All animal treatments were approved (approval no. WDRM-20200604) by the Laboratory Animal Welfare and Ethics Committee of Renmin Hospital of Wuhan University (Wuhan, China). The mice were kept under specific pathogen-free conditions and in a steady temperature (22±2˚C) and humidity (40-70%) barrier system with a 12-h light/dark cycle, and food and water available.

Study design. The 18 mice were divided randomly into three groups (n=6 per group), namely, the control (Con), CaOx stone, and CaOx stone + Fer-1 group (CaOx + Fer-1). The CaOx stone model in the kidneys of mice was established with intraperitoneal injection of 80 mg/kg glyoxylic acid (Sigma-Aldrich; Merck KGaA) for 14 days (15); 5 mg/kg Fer-1 (inhibitor of ferroptosis; MedChemExpress) was injected once daily for 3 consecutive days before glyoxylic acid treatment and seventh after modeling (16). Mice in the control group received an intraperitoneal injection of saline solution. The experimental mice were anesthetized by intraperitoneal injection of pentobarbital (50 mg/kg) for renal tissue and blood sampling. The blood was centrifuged (4,000 x g) for 15 min at 4˚C to obtain the serum, and the kidneys were harvested and then stored at -80˚C or fixed in paraformaldehyde solution. All animals were sacrificed with pentobarbital (100 mg/kg) after surgery.

Cell culture. Human proximal tubular cells (HK-2 cells; cat. no. SCSP-511) were obtained from the Cell Bank of the Chinese Academy of Sciences, maintained in complete DMEM/F12 with 10% fetal bovine serum (Gibco; Thermo Fisher Scientific, Inc.), 1% penicillin and streptomycin and cultured at 37˚C in an incubator with 5% CO_2. Ox (Sigma-Aldrich; Merck KGaA) was added to the serum-free DMEM/F12 to prepare the Ox intervention solution. When cell confluence reached 80%, the cells were exposed to 2 mM Ox intervention solution for 24 h prior to analysis. Subsequently, the HK-2 cells were treated with Fer-1 (100 μM) with or without Ox intervention solution (2 mM) for 24 h at 37˚C (17).

Iron measurements. Cells ($2x10^6$) were rapidly homogenized in iron assay buffer using an Iron Assay kit (product no. MAK025; Sigma Aldrich; Merck KGaA). Briefly, iron is released by the addition of an acidic buffer. Samples were assessed to measure total iron. Released iron could react with the iron probe resulting in a colorimetric (593 nm) product, proportional to the iron present. The solution was then centrifuged at 13,000 x g for 10 min at 4˚C to remove insoluble material and was measured at 593 nm with a microplate fluorometer (Bio-Rad Laboratories, Inc.).

Cell viability assay. The cell viability after the use of Fer-1 and Ox was measured by Cell Counting Kit-8 (CCK-8; Beyotime Institute of Biotechnology) assay. Cells ($3x10^3$/well) were seeded into 96-well culture plates at 37˚C for 24 h. The cells were then co-treated with different concentrations of Fer-1 (0, 2, 4, 8, 16, 32, and 64 μM) and oxalate (2 mM) in DMEM/F12. A total of 10 μl of CCK-8 solution was added to each well and incubated at 37˚C for another 2 h. The optical density at 450 nm was determined using a microplate reader (Bio-Rad Laboratories, Inc.).

Hematoxylin-eosin (H&E) staining. The kidney tissue (fixed with 4% paraformaldehyde solution at 26˚C) was dehydrated with gradient ethanol, embedded in paraffin, cut into 4-μM sections, subjected to xylene dewaxing and gradient ethanol debenzylation, and washed with distilled water. The tissues were stained with hematoxylin for 5 min and eosin for 1 min at room temperature using the H&E staining kit (cat. no. C0105; Beyotime Institute of Biotechnology) and injuries were scored as follows: 0, no tubular injury; 1, <10% tubular damage; 2, 10-25% tubular damage; 3, 26-50% tubular damage; 4, 51-74% tubular damage; and 5, >75% tubular damage.

Immunofluorescence staining for kidney tissue. Renal tissues were fixed in 4% paraformaldehyde at 4˚C for 24 h, embedded in paraffin and cut into 4-μm sections. The sample was then washed with pure water, and the slices were transferred into 0.01 M citrate buffer (pH 6.0), heated in a microwave oven for antigen repair, and repaired with medium and high temperatures for 2-8 min. The specific time was adjusted according to the actual situation of the sample. Subsequently, the sample was cooled to room temperature, and a circle was drawn around the tissue with a histochemical pen to prevent the incubation solution from flowing away in the later process. PBS was used to wash the sample thrice for 5 min each time. The primary antibody: α-Smooth muscle actin (α-SMA; 1:200;

cat. no. BM0002; Wuhan Boster Biological Technology, Ltd.), fibronectin (1:400; cat. no. 15613-1-AP; ProteinTech Group, Inc.), E-cadherin (1:500; cat. no. 40772; Abcam), GPX4, (1:200; cat. no. 6701; Affinity Biosciences, Ltd.), SLC7A11 (1:200; cat. no. 26864; ProteinTech Group, Inc.), and superoxide dismutase 2 (SOD2; 1:200; cat. no. 13534; Abcam) was incubated with 5% BSA 4˚C overnight. The sample was reheated and washed thrice with PBS for 5 min each time. An appropriate amount of secondary antibody (goat anti-rabbit HRP; 1:1,000; cat. no. A-11034; Thermo Fisher Scientific, Inc.) working solution was added to the slices, and the sample was incubated in a water bath at 37˚C for 30 min in the dark and washed thrice with PBS for 5 min each time. DAPI was then added dropwise to stain the nuclei, and the mixture was incubated in the dark at room temperature for 20-30 min and washed with PBS. Finally, the film was sealed with anti-fluorescence quenching sealing agent. All images were observed under a fluorescence microscope (Nikon Corporation) and figures were analyzed using ImageJ software (version 1.8.0; National Institutes of Health).

Immunohistochemistry (IHC) analysis. In brief, 4-μm paraffin-embedded sections were deparaffinized, subjected to antigen retrieval using citrate buffer (pH 6.0) at 95˚C for 10 min and treated with 0.3% H_2O_2 to block their endogenous peroxidase activity at room temperature for 10 min. Next, the sections were continuously treated with blocking reagent QuickBlock™ (cat. no. P0260; Beyotime Institute of Biotechnology), then incubated with the primary antibody for kidney injury molecular 1 (KIM-1; 1:100) at 4˚C overnight, and then with the secondary antibody (1:5,000; cat. no. TA130017; biotinylated goat anti-rabbit; OriGene Technologies, Inc.) for 1 h at room temperature. Peroxidase activity was visualized using 3,3'-diaminobenzidine at room temperature for 5 min. The positive stained areas of KIM-1, based on the unit area (magnification, x400), were calculated as the percentage of all examined areas using ImageJ software (version 1.8.0; National Institutes of Health).

TUNEL assay. A TUNEL assay kit (cat. no. MK1015; Wuhan Boster Biological Technology, Ltd.) was used to detect apoptotic cells according to the manufacturer's instructions. Kidney paraffin sections were incubated overnight at 4˚C with anti-neuronal nuclei antibody (cat. no. BM4354; 1:100; Wuhan Boster Biological Technology, Ltd.) according to the manufacturer's instructions. The sections were incubated with TUNEL reaction mixture for 1 h at 37˚C before being rinsed three times with PBS. Images were captured using an inverted fluorescence microscope at high magnification (x400). TUNEL-positive neurons in five randomly selected areas surrounding the injury site were quantified, and the data were analyzed using ImageJ software (version 1.8.0; National Institutes of Health).

Hoechst staining. Hoechst 33342/PI double staining was used for morphological analysis. Cells were plated in replicates at $1x10^6$ cells per well in 6-well plates. The cells were collected via centrifugation at 300 x g for 5 min at 25˚C, suspended in cell staining buffer, and incubated with 5 μl Hoechst 33342 and 5 μl PI solution (cat. no. CA1120; Beijing Solarbio Science & Technology Co., Ltd.) at 4˚C for 30 min. All images were observed under a fluorescence microscope (Nikon Corporation) and figures were analyzed using ImageJ software (version 1.8.0; National Institutes of Health).

Masson staining. Renal tissues were fixed in 4% paraformaldehyde at 4˚C for 24 h, embedded in paraffin and cut into 4-μm sections. Then, a circle was drawn around the tissue with a histochemical pen to prevent the incubation solution from flowing away in the later process. Subsequently, the sample was washed thrice with pure water for 5 min each time. By using the Masson staining kit (Wuhan Servicebio Technology Co., Ltd.), solution A was added, and the solution was soaked at room temperature overnight. The slices soaked in liquid were placed into the oven at 62˚C for 30 min, and liquids D and F were added for preheating. The sample was then washed with tap water until the yellow dye on the tissue was no longer evident. Equal quantities of liquids B and C were added to dye the samples for 1 min at room temperature, and were then washed with tap water. Following differentiation with 1% hydrochloric acid and alcohol for 1 min, the nucleus was gray black, and the background was almost colorless. The sample was washed with tap water and dyed with solution D for 6 min, washed with water, and then dyed with solution E for 1 min at room temperature. Without washing, the sample was dyed with solution F for 8-15 sec at room temperature. Finally, 1% glacial acetic acid was differentiated thrice for several seconds. Renal fibrosis was verified using Masson trichrome staining (blue area). All images were observed under a light microscope (Nikon Corporation) and figures were analyzed using ImageJ software (version 1.8.0; National Institutes of Health).

Sirius red staining. Renal tissues were fixed in 4% paraformaldehyde at 4˚C for 24 h, embedded in paraffin and cut into 4-μm sections. Then, a circle was drawn around the tissue with a histochemical pen to prevent the incubation solution from flowing away in the later process. The sample was washed thrice with pure water for 5 min each time. Subsequently, Sirius red staining was carried out for 30 min at room temperature. The slices were directly divided into absolute ethanol for several seconds. Renal fibrosis was verified using Sirius red staining (red area). All images were observed under a light microscope (Nikon Corporation) and figures were analyzed using ImageJ software (version 1.8.0; National Institutes of Health).

Von Kossa staining. Renal tissues were fixed in 4% paraformaldehyde at 4˚C for 24 h, embedded in paraffin and cut into 4-μm sections. The sections were then placed in 1% silver nitrate solution under ultraviolet light for 45 min. Subsequently, the sample was washed with distilled water, treated with 3% sodium thiosulphate for 5 min at room temperature, and washed with water. Finally, the sample was counterstained with van Gieson for 5 min at room temperature and washed with alcohol. The crystal deposition area (black area) was quantified using ImageJ software (version 1.8.0; National Institutes of Health).

Western blotting. Renal tissue homogenates and cell lysates were prepared in RIPA buffer containing phenylmethylsulfonyl fluoride and a phosphatase inhibitor cocktail (Wuhan

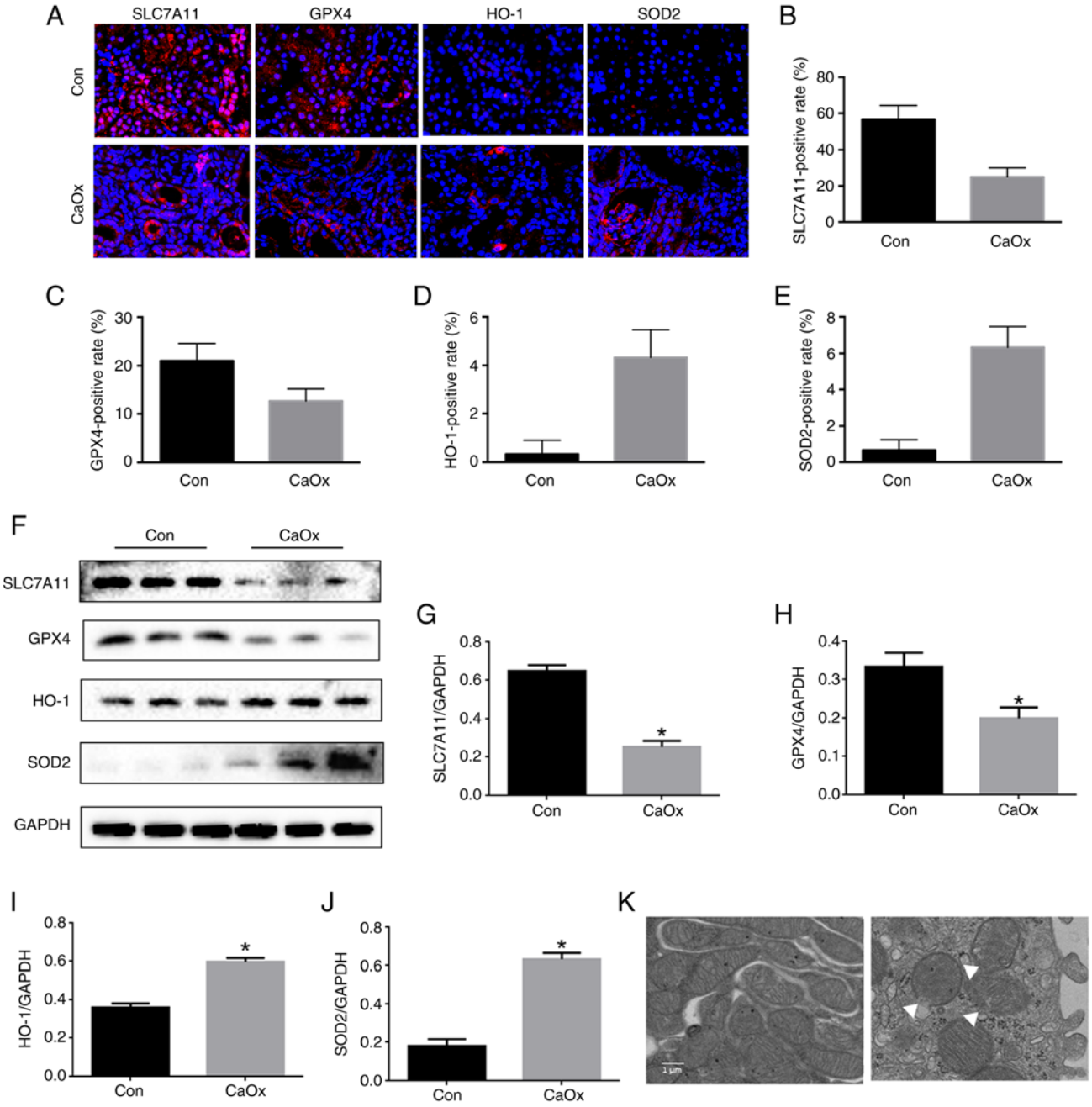

Figure 1. Activation of ferroptosis in mouse kidneys with CaOx stones. (A) Renal cortex expression of SLC7A11, GPX4, HO-1 and SOD2 determined by immunofluorescence staining in mice after glyoxylic acid treatment (magnification, x400). (B-E) Quantification of (B) SLC7A11, (C) GPX4, (D) HO-1 and (E) SOD2 in mouse kidneys assessed using immunofluorescence. (F) Western blot analysis of SLC7A11, GPX4, HO-1 and SOD2 in renal tissue lysates from these groups. (G-J) The ratio of the optical density of (G) SLC7A11, (H) GPX4, (I) HO-1, and (J) SOD2 to GAPDH was statistically analyzed. (K) Representative images of mitochondrial injury under glyoxylic acid treatment were observed by TEM. White triangles represent the injured mitochondria. The data are presented as the mean ± SD; n=6. *P<0.05 vs. the control group. CaOx, calcium oxalate; SLC7A11, solute carrier family 7 member 11; GPX4, glutathione peroxidase 4; HO-1, heme oxygenase 1; SOD2, superoxide dismutase 2; TEM, transmission electron microscopy.

Servicebio Technology Co., Ltd.). The protein content was measured using a bicinchoninic acid assay (Bio-Rad Laboratories, Inc). After BCA quantification, 30 μg protein samples were obtained from each hole, separated by 10% SDS-PAGE gel electrophoresis, and transferred to polyvinylidene fluoride membranes. The membrane was sealed with 5% milk for 1 h at 26˚C, and then with 0.5% skim. It was then washed thrice using Tris-buffered saline containing 1% Tween-20 (TBST) for 10 min each time. The membrane was then incubated with a primary antibody: SOD2 (1:1,000; cat. no. ab137037; Abcam), heme oxygenase 1 (HO-1; 1:2,000; cat. no. ab52947; Abcam), GPX4 (1:1,000; cat. no. DF6701; Affinity Biosciences, Ltd.), SLC7A11 (1:1,000; cat. no. DF12509; Affinity Biosciences, Ltd.), caspase-3 (1:2,000; cat. no. AF7022; Affinity Biosciences, Ltd.), fibronectin (1:1,000; cat. no. sc-8422; Santa Cruz Biotechnology, Inc.), E-cadherin (1:5,000; cat. no. 20874-1; ProteinTech Group, Inc.), vimentin (1:5,000; cat. no. 10366-1; ProteinTech Group, Inc.), α-SMA (1:1,000; cat. no. BM0002; Wuhan Boster Biological Technology, Ltd.) and GAPDH (1:5,000;

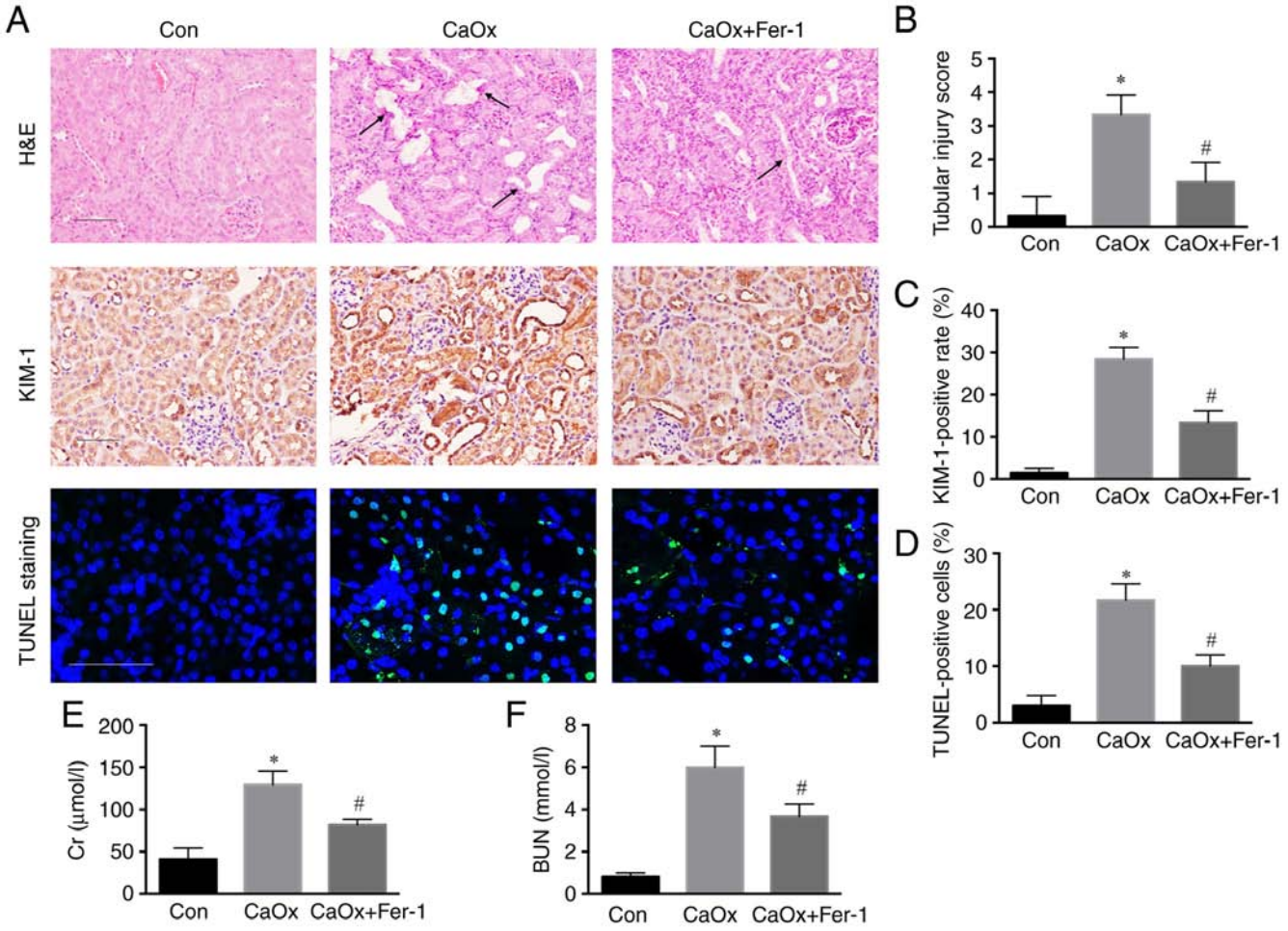

Figure 2. Fer-1 inhibits renal injury induced by CaOx stones. (A) Representative images of the renal cortex by H&E staining, immunohistochemical staining (magnification, x200) and TUNEL assay (magnification, x400) following Fer-1 treatment. Black arrows represent the injured renal tubule. (B) Tissue injury scores in each group were statistically analyzed. (C) Semi-quantitative statistical analysis of KIM-1. (D) Quantification of renal apoptosis by TUNEL assay. (E and F) Serum BUN and Cr levels of three groups following Fer-1 treatment. The data are presented as the mean ± SD; n=6. *P<0.05 vs. the control group; #P<0.05 vs. the CaOx group. Fer-1, ferrostatin-1; CaOx, calcium oxalate; H&E, hematoxylin and eosin; TUNEL, terminal deoxynucleotidyl transferase-mediated dUTP nick end labeling; KIM-1, kidney injury molecule-1; BUN, blood urea nitrogen; Cr, creatinine.

cat. no. 60004-1; ProteinTech Group, Inc.) overnight at 4˚C. The sample was then washed thrice with TBST for 10 min each time. The membrane was removed and incubated with the secondary antibody (1:1,000; cat. no. SA00001-2; ProteinTech Group, Inc.) at 37˚C for 2 h. TBST was then used to wash the membrane for 10 min each time. Finally, ECL (cat. no. BL520A; Biosharp Life Sciences) color was developed with GAPDH as an internal reference to analyze the protein expression level on the membrane. ImageJ software (version 1.8.0; National Institutes of Health) was used to semi-quantify protein expression with GAPDH as the loading control.

Detection of ROS by flow cytometry. Intracellular ROS production was detected using the probe DCF-DA (Beyotime Institute of Biotechnology). Cells (3x10^6/well) were seeded in a 6-well plate and stimulated by Ox, followed by incubation with 10 μM DCF-DA for 20 min at 37˚C. The cells were then collected and washed with PBS. After resuspending the pellet in 200 μl PBS, fluorescence was detected using a BD Accuri C6 Plus flow cytometer and FACSDiva software (version 6.13) (BD Biosciences).

Transmission electron microscopy (TEM). The kidney tissues were fixed for 2 h with 2.5% glutaraldehyde in a 0.05 M sodium cacodylate buffer at pH 7.2 and at 25˚C, followed by 2 h in 2% OsO_4 in a 0.1 M sodium cacodylate buffer and 18 h in 1% aqueous uranyl acetate. Following dehydration through an ethanol series, the specimens were embedded in epoxy resin 618 at 40˚C and cut into 60-80 nm ultrathin sections and then subjected to uranium lead double staining at 4˚C for 20 min. TEM (Hitachi, Ltd.) was used to observe renal tubular epithelial cells and for image acquisition.

Assessment of blood urea nitrogen (BUN) and (creatinine) Cr. Renal tissues and blood were collected for biochemical analysis. BUN and Cr serum levels in renal tissues were assessed using the corresponding detection kits (cat. no. C011-2 and C013-1; Nanjing Jiancheng Bioengineering Institute) in accordance with the manufacturer's instructions.

Statistical analysis. Statistical analysis of the data was performed using GraphPad Prism 5.0 (GraphPad Software, Inc.). The data are presented as the mean ± standard deviation. The unpaired Student's t-test was used to compare the mean

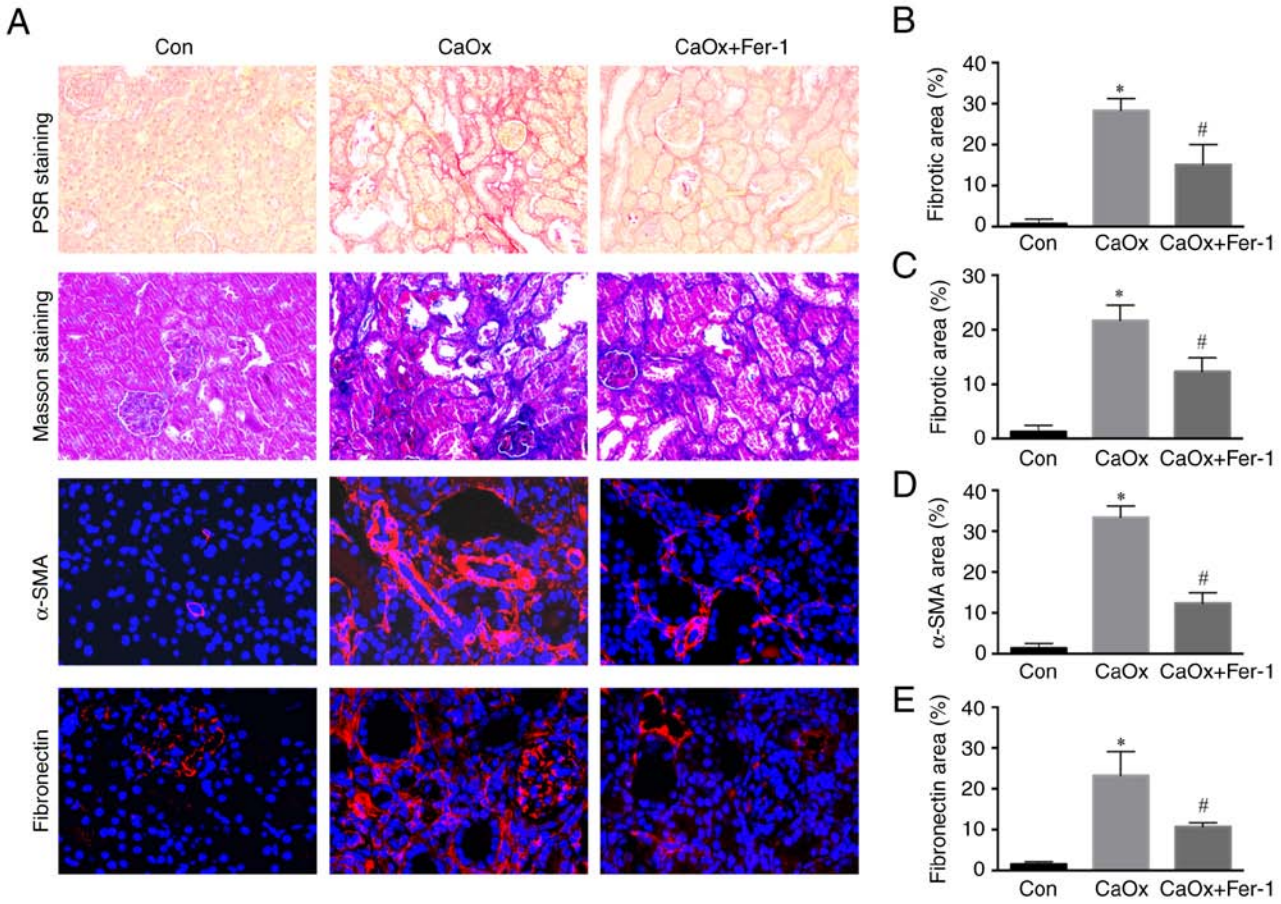

Figure 3. Ferrostatin-1 inhibits renal fibrosis after renal injury induced by CaOx stones. (A) Representative images of Masson's staining (blue), Sirius red staining (red), immunofluorescence staining of fibronectin and α-SMA (red) in renal tissue (magnification, x400). (B) Quantification of renal fibrosis by Sirius red staining. (C) Quantification of renal fibrosis by Masson's staining. (D) Quantification of α-SMA in mouse kidneys assessed by immunofluorescence staining. (E) Quantification of fibronectin in mouse kidneys assessed by immunofluorescence staining. The data are presented as the mean ± SD; n=6. *P<0.05 vs. the control group; #P<0.05 vs. the CaOx group. CaOx, calcium oxalate; α-SMA, α-smooth muscle actin; PSR, Picrosirius red; Fer-1; ferrostatin-1.

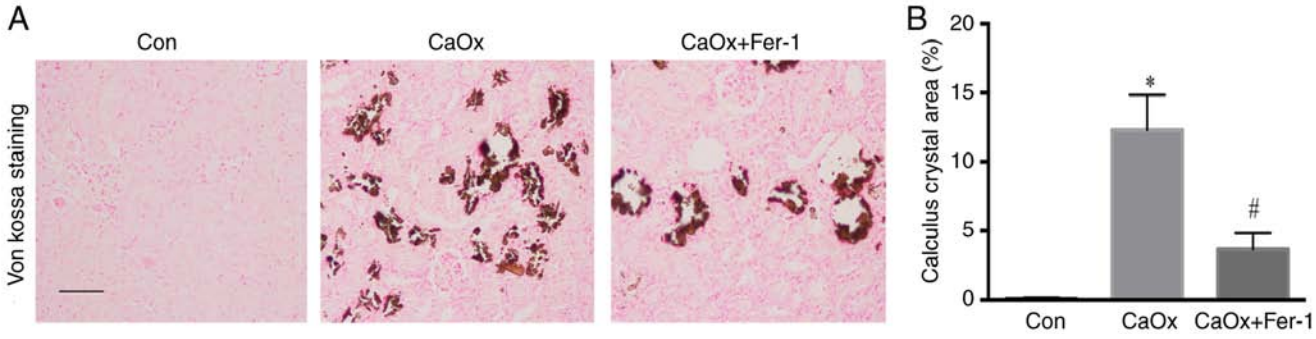

Figure 4. Ferrostatin-1 inhibits CaOx stone formation. (A) Histopathological analysis of Von Kossa staining (magnification, x200). (B) Quantification analysis of stone deposition by Von Kossa staining. The data are presented as the mean ± SD; n=6. *P<0.05 vs. the control group; #P<0.05 vs. the CaOx group. CaOx, calcium oxalate.

values between two groups. One-way analysis of variance and Bonferroni's post hoc test were used to evaluate the differences among groups. P<0.05 was considered to indicate a statistically significant difference.

Results

Activation of ferroptosis in the CaOx kidney stone mouse model. To explore the role of ferroptosis in CaOx stones, a CaOx kidney stone mouse model was established with intraperitoneal injection of 80 mg/kg glyoxylic acid for 14 days. Through immunofluorescence staining of kidney tissue, the levels of SLC7A11 and GPX4 were revealed to be significantly decreased (Fig. 1A-C), and the levels of SOD2 and HO-1 in renal tissue in the CaOx group were significantly increased (Fig. 1A, D and E). Through western blotting of kidney tissue, the levels of SLC7A11 and GPX4 were revealed to be significantly decreased (Fig. 1F-H), and the levels of SOD2 and HO-1 in renal tissue in the CaOx

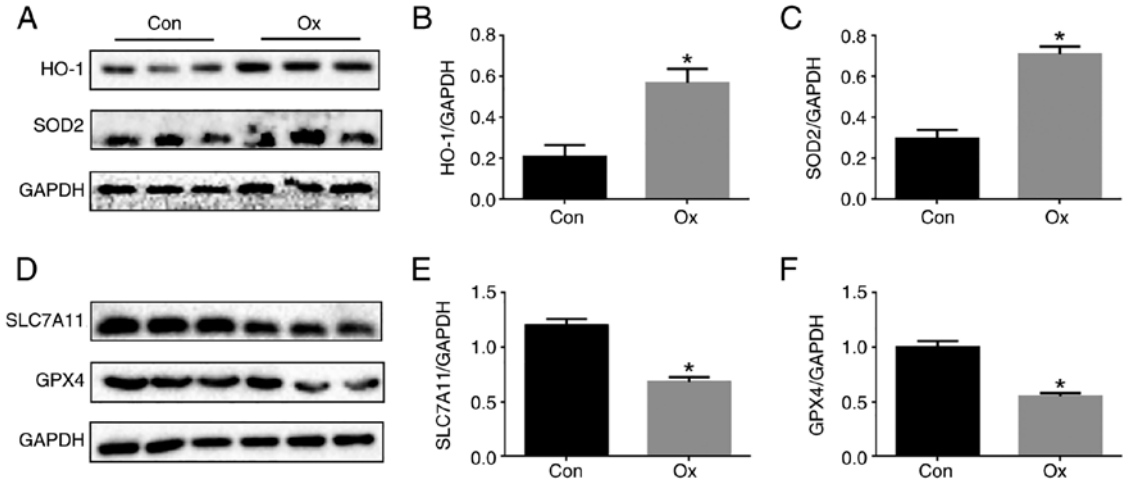

Figure 5. Activation of ferroptosis in Ox-induced injury of HK-2 cells. Cells were exposed to 2 mM Ox intervention solution for 24 h. (A) Western blot analysis of HO-1 and SOD2 in Ox-induced injury of renal tubular epithelial cells. (B and C) The ratio of the optical density of (B) HO-1 and (C) SOD2 to GAPDH was statistically analyzed. (D) Western blot analysis of SLC7A11 and GPX4 in Ox-induced injury of renal tubular epithelial cells. The ratio of the optical density of (E) SLC7A11 and (F) GPX4 to GAPDH was statistically analyzed. The data are presented as the mean ± SD; n=3. *P<0.05 vs. the control group. Ox, oxalate; HO-1, heme oxygenase 1; SOD2, superoxide dismutase 2; SLC7A11, solute carrier family 7 member 11; GPX4, glutathione peroxidase 4.

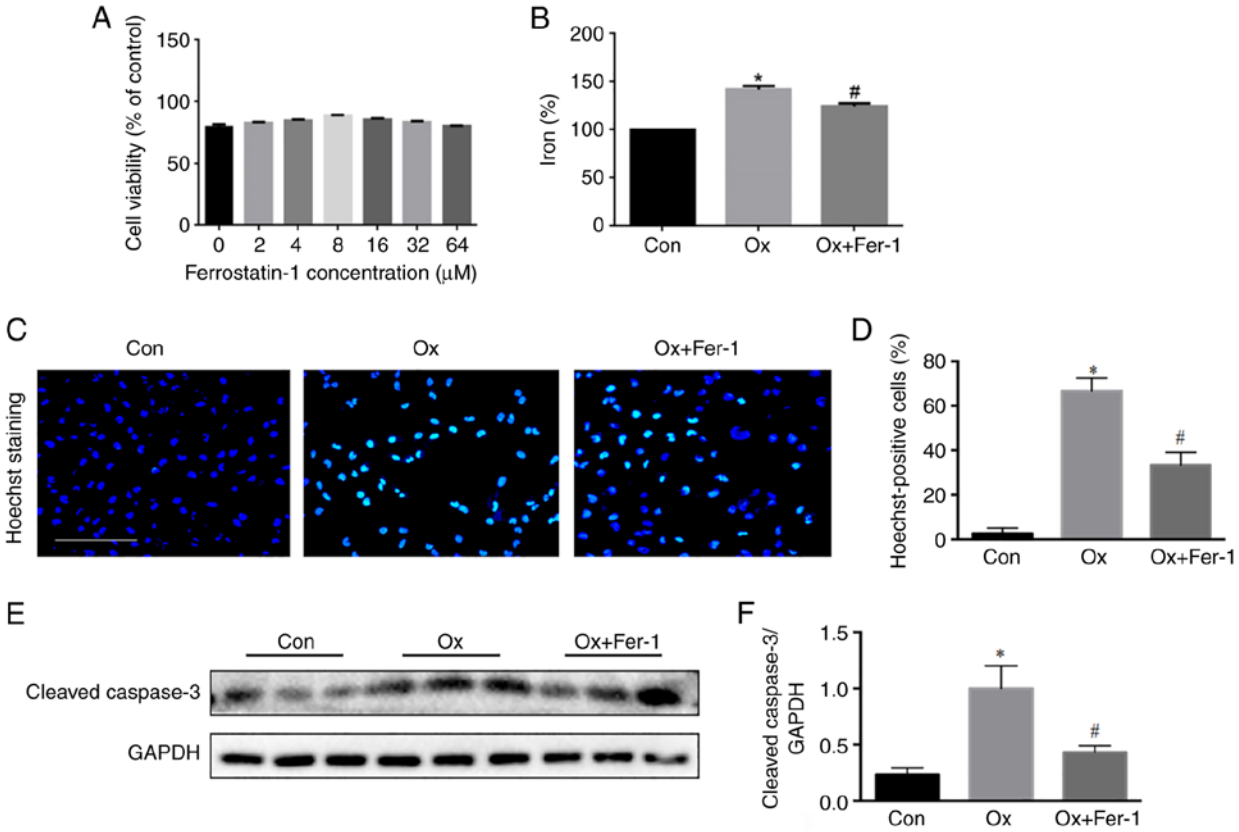

Figure 6. Fer-1 inhibits Ox-induced apoptosis of HK-2 cells. (A) Cells were incubated with various concentrations of Fer-1 (0, 2, 4, 8, 16, 32 and 64 μmol/l) and Ox (2 mM) and cell viability was assessed by CCK-8 assay. (B) Intracellular iron levels in HK-2 cells. (C) Representative images of HK-2 cells by Hoechst staining (green) after Fer-1 treatment. (D) Quantification of HK-2 cells apoptosis by Hoechst staining. (E) Representative images cleaved caspase-3 in HK-2 cells. (F) Quantification of cleaved caspase-3 in HK-2 cells assessed by western blotting. The data are presented as the mean ± SD; n=3. *P<0.05 vs. the control group; #P<0.05 vs. the Ox group. Fer-1, ferrostatin-1; Ox, oxalate; CCK-8, Cell Counting-Kit-8.

group were significantly increased (Fig. 1F, I and J). By using TEM, it was observed that compared with the control group, the mitochondrial morphology in the CaOx group exhibited the characteristic changes of ferroptosis, including the vanishing of mitochondria cristae and rupture of the outer mitochondrial membrane (Fig. 1K). Therefore, ferroptosis occurred in the mouse kidney of CaOx stone.

Fer-1 inhibits renal injury induced by CaOx stones. Fer-1 acts as a specific inhibitor of ferroptosis, which plays an important

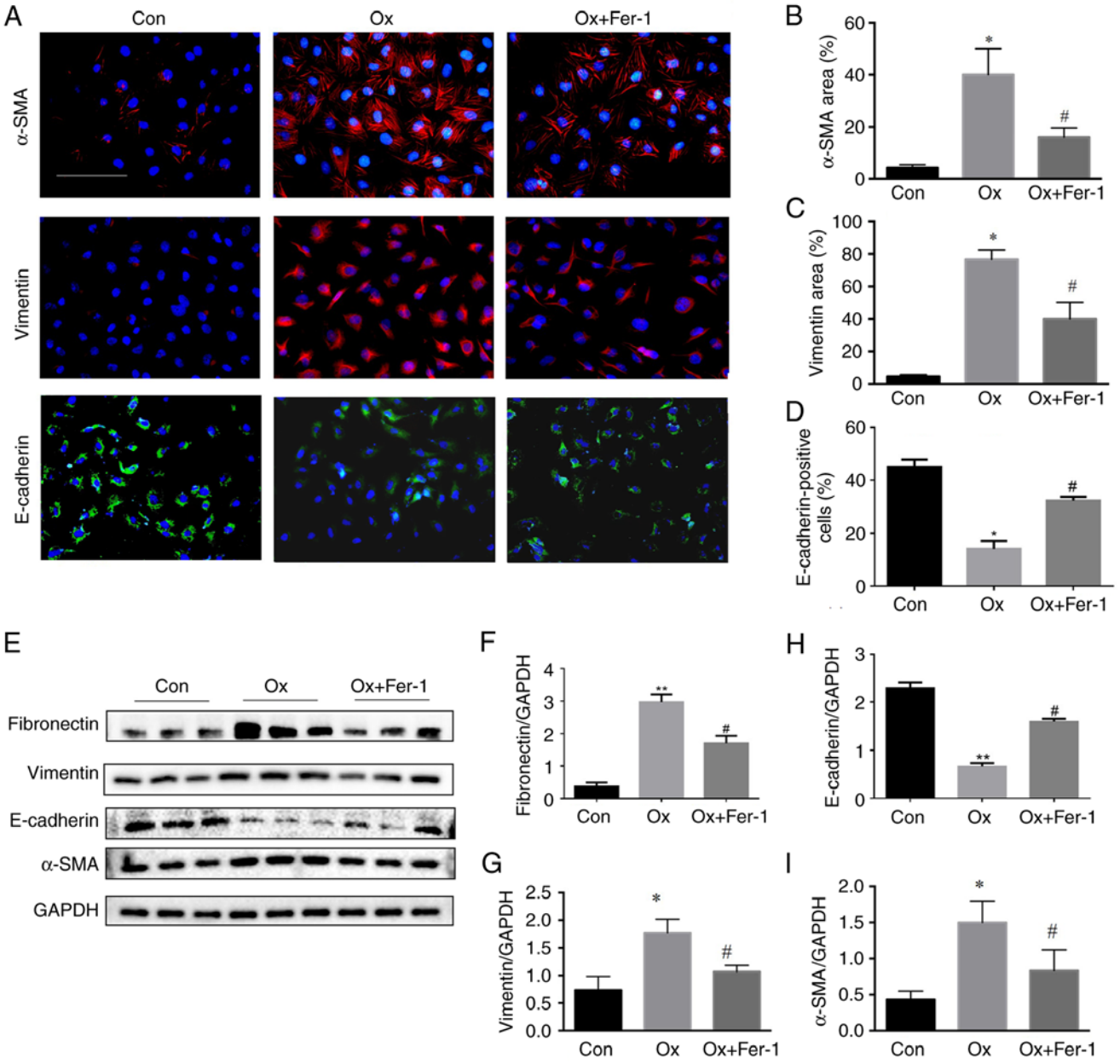

Figure 7. Fer-1 inhibits EMT and renal fibrosis following Ox-induced injury of HK-2 cells. Cells were treated with Fer-1 with or without Ox intervention solution for 24 h. (A) Representative images of immunofluorescence staining of α-SMA, vimentin (red) and E-cadherin (green) (magnification, x400) following Fer-1 treatment. (B-D) Semi-quantitative statistical analysis of (B) α-SMA, (C) vimentin and (D) E-cadherin. (E) Representative images of fibronectin, vimentin, α-SMA and E-cadherin in HK-2 cells by western blotting. (F-I) Quantification of (F) fibronectin, (G) vimentin, (H) E-cadherin and (I) α-SMA in HK-2 cells assessed by western blotting. The data are presented as the mean ± SD; n=3. *P<0.05 vs. the control group; #P<0.05 vs. the Ox group. Fer-1, ferrostatin-1; EMT, epithelial-mesenchymal transition; Ox, oxalate; α-SMA, α-smooth muscle actin,

role in various diseases. H&E staining revealed a higher injury score of renal tubules in the CaOx group than in the control group. Following Fer-1 treatment, renal tubular injury was decreased compared with the CaOx group (Fig. 2A and B). Through immunohistochemical staining of kidney tissue, the level of KIM-1 was revealed to be significantly increased compared with the control group, and the level of KIM-1 in renal tissue in the CaOx + Fer-1 group was significantly decreased compared with that of the CaOx stone group (Fig. 2A and C). Terminal deoxynucleotidyl transferase-mediated dUTP nick end labeling (TUNEL staining) revealed a higher rate of apoptosis of renal tubules in the CaOx model group compared with the control group, and renal tubular apoptosis was decreased in the CaOx + Fer-1 treatment group compared with that of the CaOx stone group (Fig. 2A and D). Moreover, serum BUN and Cr levels were increased compared with the control group and decreased in the CaOx + Fer-1 treatment group compared with those of the CaOx stone group (Fig. 2E and F).

Fer-1 inhibits renal fibrosis after renal injury induced by CaOx stones. Renal injury is closely associated with the increased risk of developing CKD, and the risk of CKD incidence is dependent on the severity of renal injury (18). The results of Picrosirius red (PSR) staining showed that renal fibrosis in the CaOx group was increased compared with the control group. Following Fer-1 treatment, renal fibrosis

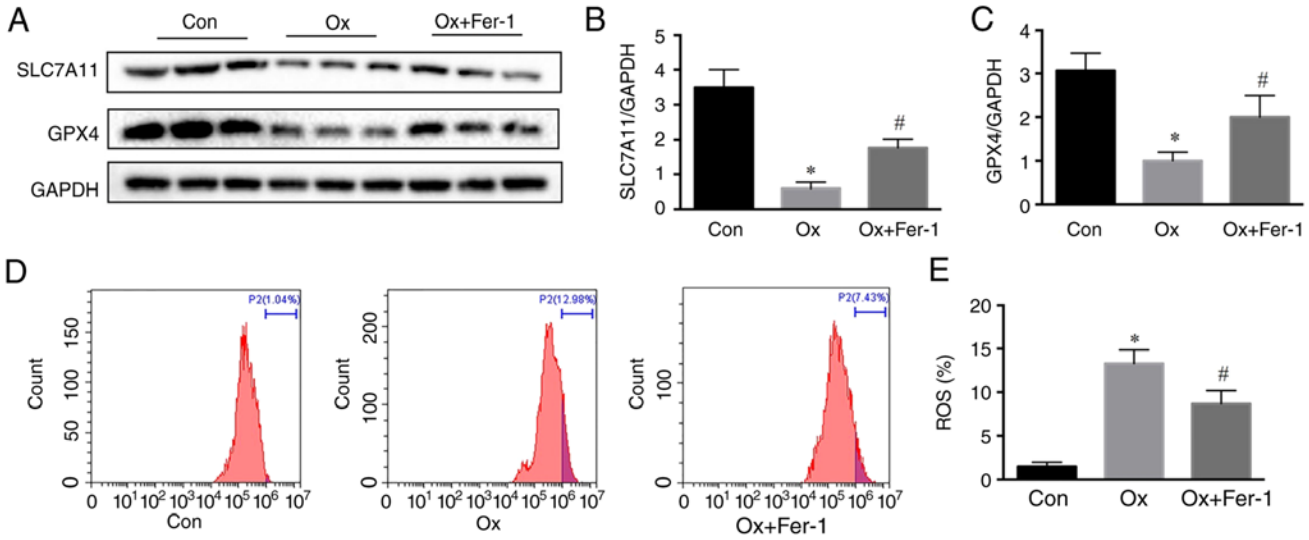

Figure 8. Fer-1 inhibits renal fibrosis following Ox-induced injury of HK-2 cells via inhibition of ferroptosis. Cells were treated with Fer-1 with or without Ox intervention solution for 24 h. (A) Western blot analysis of SLC7A11 and GPX4 in HK-2 cells following Fer-1 treatment. (B and C) Quantification of (B) SLC7A11 and (C) GPX4 in HK-2 cells assessed by western blotting. (D) ROS levels in HK-2 cells following Fer-1 treatment. (E) Quantification of ROS in HK-2 cells. The data are presented as the mean ± SD; n=3. *P<0.05 vs. the control group; #P<0.05 vs. the Ox group. Fer-1, ferrostatin-1; Ox, oxalate; SLC7A11, solute carrier family 7 member 11; GPX4, glutathione peroxidase 4; ROS, reactive oxygen species.

in mice was significantly lower than that in the CaOx group (Fig. 3A and B). Similarly, Masson staining revealed that renal fibrosis in the CaOx group was significantly increased compared with the control group. Following Fer-1 treatment, renal fibrosis in mice was significantly lower than that in the CaOx group (Fig. 3A and C). Through immunofluorescence staining of kidney tissue, the levels of fibronectin and α-SMA in renal tissue of the CaOx group were revealed to be significantly increased compared with the control, whereas the levels of fibronectin and α-SMA were significantly decreased in the CaOx + Fer-1 treatment group compared with the levels in the CaOx group (Fig. 3A, D and E).

Fer-1 inhibits CaOx stone formation. Von Kossa staining showed that CaOx crystals were deposited in the renal interstitium of mice in the CaOx group. Following Fer-1 treatment, the CaOx crystals in mice were significantly lower than those in the CaOx group (Fig. 4).

Activation of ferroptosis in Ox induces injury of renal tubular epithelial cells. This experiment aimed to further explore the role of ferroptosis in the Ox-induced injury of renal tubular epithelial cells. Western blot analysis revealed that the levels of HO-1 and SOD2 in tubular cells in the Ox group were significantly increased (Fig. 5A-C), and the levels of GPX4 and SLC7A11 were significantly decreased compared with the control group (Fig. 5D-F). Therefore, ferroptosis occurred in the Ox-induced injury of renal tubular epithelial cells.

Fer-1 inhibits Ox-induced injury of renal tubular epithelial cells. Renal tubular epithelial cells were treated with different concentrations of Fer-1 and 2 mM Ox to explore the function of Fer-1 in Ox-induced renal tubular epithelial cell injury. It was determined that the peak protective dose of Fer-1 was 8 μM (P<0.01). Therefore, co-culturing with 8 μM Fer-1 and 2 mM Ox was used in the present study (Fig. 6A). The intracellular iron level was significantly increased under the stimulation of Ox and decreased following the Fer-1 treatment (Fig. 6B). Hoechst staining revealed a higher apoptotic rate of renal tubules in the Ox group than in the control group. Following Fer-1 treatment, the renal tubular apoptotic rate was decreased compared with the Ox group (Fig. 6C and D). The results of western blot analysis of caspase-3 revealed a higher rate of apoptosis of renal tubules in the Ox group compared with the control group, and renal tubular apoptosis was decreased in the Ox + Fer-1 group compared with the Ox group (Fig. 6E and F).

Fer-1 inhibits epithelial-mesenchymal transition (EMT) and renal fibrosis following Ox-induced injury of renal tubular epithelial cells. Through immunofluorescence staining of kidney tissue, the levels of vimentin and α-SMA were revealed to be significantly increased in the Ox group while the levels of E-cadherin were significantly decreased, compared with the control group. In addition, the levels of vimentin and α-SMA were significantly decreased, and the levels of E-cadherin were significantly increased in the Ox + Fer-1 treatment group compared with the Ox group (Fig. 7A-D). The results of western blot analysis revealed that the levels of fibronectin, vimentin and α-SMA were significantly increased and E-cadherin was decreased in the Ox group, compared with the control group. Furthermore, the levels of fibronectin, vimentin and α-SMA were significantly decreased and E-cadherin was increased in the Ox + Fer-1 treatment group compared with the Ox group (Fig. 7E-I).

Fer-1 inhibits renal fibrosis after Ox-induced injury of renal tubular epithelial cells via inhibition of ferroptosis. The ferroptosis level in renal tubular epithelial cells was evaluated to analyze the effect of Fer-1. The expression levels of both SLC7A11 and GPX4 were increased in the Ox + Fer-1 group

compared with the Ox group (Fig. 8A-C). Furthermore, the levels of ROS were highest in the Ox group, followed by the Ox + Fer-1 and control group (Fig. 8D and E). Therefore, Fer-1 alleviated Ox-induced injury of renal tubular epithelial cells by inhibiting ferroptosis, which plays a key role in renal fibrosis.

Discussion

Ferroptosis is a new type of non-apoptotic programmed cell death characterized by iron-dependent lipid peroxidation, which is closely related to the occurrence of blood, neurological, respiratory, cardiovascular, and reproductive system diseases and tumors (19-21). However, related studies on the role of ferroptosis in urinary system diseases have mainly focused on renal failure and renal tumors (22,23), and to date, limited studies are available on the topic of urolithiasis formation and the progression of patients with urolithiasis to CKD. The present study, to the best of our knowledge, is the first to explore the pathogenic mechanism of ferroptosis in Ox-induced renal tubular epithelial cell injury and fibrosis and the role of inhibiting ferroptosis in improving Ox-induced renal tubular epithelial cell injury and fibrosis. The mechanism of fibrosis following CaOx stone renal injury was clarified and the progression of patients with CaOx stones to CKD was delayed. An *in vivo* CaOx stone animal model was established using glyoxylic acid and Ox-induced renal tubular epithelial cell injury and fibrosis were also established *in vitro*. The results of the experiments demonstrated that Ox promoted lipid peroxidation. Moreover, Ox activated the ferroptosis-related signaling pathway proteins (HO-1 and SOD2) and decreased the relative expression levels of SLC7A11 and GPX4. Thus, renal tubular epithelial cell injury and the degree of ferroptosis exhibited a positive association with Ox.

To further investigate the association between ferroptosis and injury to renal tubular epithelial cells induced by exposure to Ox, the ferroptosis inhibitor, Fer-1, was used. Fer-1 is the first ferroptosis inhibitor, and is widely used *in vitro* and *in vivo* (13,24). The function of Fer-1 against ferroptosis mainly depends on the inhibition of lipid peroxidation (25). In the present study, Fer-1 was applied in both *in vitro* and *in vivo* models and exhibited a marked effect against ferroptosis. Fer-1 significantly decreased the relative expression of the ferroptosis-promoting signaling pathway proteins, HO-1 and SOD2, and induced the relative expression of the ferroptosis-inhibiting signaling pathway proteins, SLC7A11 and GPX4. Ox could induce ferroptosis, and the increase in ferroptosis levels aggravated lipid peroxidation levels, leading to an overload of ROS in cells and an increase in the degree of cell injury. In addition, a previous study revealed that ferroptosis and apoptosis are closely linked, that apoptosis can be converted to ferroptosis under certain conditions, and that ferroptosis promotes the susceptibility of cells to apoptosis (26). By reducing the degree of ferroptosis, the damage and death of tubular cells could be reduced, and this damage to renal tubular epithelial cells plays a vital role in the formation of CaOx kidney stones (17). Consistent with the results of the present study, with the increase in the degree of ferroptosis, the deposition of crystals in the kidneys significantly increased as was determined by performing Von Kossa staining. These data confirm the promotive effect of ferroptosis in the formation of urolithiasis.

Ferroptosis participates in various pathological models of kidney injury, and *in vivo* and *in vitro* experiments have revealed that ferroptosis inhibitors are effective against kidney injury (27,28). Mice with GPX4 deletion could spontaneously develop kidney injury, while GPX4 upregulation prevented kidney injury (12). In the kidneys, lipid peroxidation is an important factor that contributes to the aggravation of kidney injury, particularly in kidney injury induced by ischemia-reperfusion (29). Hence, classical ferroptosis inhibitors can interfere with key molecules in the ferroptosis signaling pathway to resist kidney injury. Notably, ferroptosis inhibitors are effective against Ox-induced kidney injury *in vivo* and *in vitro* (30,31).

Ferroptosis is involved in multiple pathological conditions, including renal injury. However, whether ferroptosis is induced during renal fibrosis and its potential role in renal fibrosis have not been studied. Repeated and severe episodes of kidney injury are recognized as major risk factors for the development of CKD (32). The inhibition of ferroptosis can mitigate renal fibrosis in CKD rats by inhibiting TGF-β1/Smad3, inflammation, and oxidative stress pathways (33). Ferroptosis played an important role in unilateral ureteral obstruction (UUO)-induced renal fibrosis, and the ferroptosis inhibitor attenuated UUO-induced kidney fibrosis by inhibiting ferroptosis-mediated tubular cell death (34). The ferroptosis-dependent mechanisms, including GPX4 depletion, lipid peroxidation, ferritinophagy, and p53, are involved in liver and pulmonary fibrosis (35,36), and non-targeted agents that regulate the ferroptosis signaling pathway also exhibit antifibrotic effects (37). Therefore, the perspective that ferroptosis is considered a therapeutic target for organ fibrosis has been gradually accepted. Current studies focus on the relationship between ferroptosis and Ox-induced EMT. Ferroptosis inhibitors effectively inhibit EMT (22,38).

In conclusion, ferroptosis plays an important role in Ox-induced renal tubular epithelial cell injury, fibrosis and CaOx stone formation. Moreover, Fer-1 alleviates Ox-induced renal tubular epithelial cell injury, fibrosis, and CaOx stone formation via regulating ferroptosis. Therefore, the present study demonstrated that ferroptosis, a novel form of regulated cell death, occurred in Ox-induced renal tubular epithelial cell injury, fibrosis, and CaOx stone formation. Ferroptosis could become a novel therapeutic target in Ox-induced renal tubular epithelial cell injury, fibrosis, and CaOx stone formation. Finally, a ferroptosis inhibitor may be an effective type of drug to delay the progression of patients with CaOx stones to CKD.

Acknowledgements

Not applicable.

Funding

The present study was supported by grants from the Natural Science Foundation of China (grant nos. 81800617 and 81870471) and the Science and Technology Major Project of Hubei Province (grant no. 2019AEA170).

Availability of data and materials

The datasets used during the present study are available from the corresponding author upon reasonable request.

Authors' contributions

JX, ZY and XZ conceived and designed the study. LL and ZY conducted the experiments, analyzed the data and drafted the manuscript. YX and RY participated in the data acquisition and analysis. JX and ZY confirm the authenticity of all the raw data. YR, ZY and XZ provided experimental guidance and participated in data analysis. All authors read and approved the final manuscript.

Ethics approval and consent to participate

All animal treatments were approved (approval no. WDRM-20200604) by the Laboratory Animal Welfare and Ethics Committee of Renmin Hospital of Wuhan University (Wuhan, China).

Patient consent for publication

Not applicable.

Competing interests

The authors declare that they have no competing interests.

References

1. Thongprayoon C, Krambeck AE and Rule AD: Determining the true burden of kidney stone disease. Nat Rev Nephrol 16: 736-746, 2020.
2. Buysschaert B, Aydin S, Morelle J, Gillion V, Jadoul M and Demoulin N: Etiologies, clinical features, and outcome of oxalate nephropathy. Kidney Int Rep 5: 1503-1509, 2020.
3. Lumlertgul N, Siribamrungwong M, Jaber BL and Susantitaphong P: Secondary oxalate nephropathy: A systematic review. Kidney Int Rep 3: 1363-1372, 2018.
4. Steiger S, Grill JF, Ma QY, Bäuerle T, Jordan J, Smolle M, Böhland C, Lech M and Anders HJ: Anti-transforming growth factor β IgG elicits a dual effect on CaOx crystallization and progressive nephrocalcinosis-related chronic kidney Disease. Front Immunol 9: 619, 2018.
5. Mitchell T, Kumar P, Reddy T, Wood KD, Knight J, Assimos DG and Holmes RP: Dietary oxalate and kidney stone formation. Am J Physiol Renal Physiol 316: 409-413, 2019.
6. Mulay SR and Anders HJ: Crystal nephropathies: Mechanisms of crystal-induced kidney injury. Nat Rev Nephrol 13: 226-240, 2017.
7. Black LM, Lever JM and Agarwal A: Renal inflammation and fibrosis: A double-edged sword. J Histochem Cytochem 67: 663-681, 2019.
8. Dixon SJ, Lemberg KM, Lamprecht MR, Skouta R, Zaitsev EM, Gleason CE, Patel DN, Bauer AJ, Cantley AM, Yang WS, *et al*: Ferroptosis: An iron-dependent form of nonapoptotic cell death. Cell 149: 1060-1072, 2012.
9. Mou Y, Wang J, Wu J, He D, Zhang C, Duan C and Li B: Ferroptosis, a new form of cell death: Opportunities and challenges in cancer. J Hematol Oncol 12: 34, 2019.
10. Derry PJ, Hegde ML, Jackson GR, Kayed R, Tour JM, Tsai AL and Kent TA: Revisiting the intersection of amyloid, pathologically modified tau and iron in Alzheimer's disease from a ferroptosis perspective. Prog Neurobiol 184: 101716, 2020.
11. Li Y, Feng D, Wang Z, Zhao Y, Sun R, Tian D, Liu D, Zhang F, Ning S, Yao J and Tian X: Ischemia-induced ACSL4 activation contributes to ferroptosis-mediated tissue injury in intestinal ischemia/reperfusion. Cell Death Differ 26: 2284-2299, 2019.
12. Friedmann Angeli JP, Schneider M, Proneth B, Tyurina YY, Tyurin VA, Hammond VJ, Herbach N, Aichler M, Walch A, Eggenhofer E, *et al*: Inactivation of the ferroptosis regulator Gpx4 triggers acute renal failure in mice. Nat Cell Biol 16: 1180-1191, 2014.
13. Zilka O, Shah R, Li B, Friedmann Angeli JP, Griesser M, Conrad M and Pratt DA: On the mechanism of cytoprotection by ferrostatin-1 and liproxstatin-1 and the role of lipid peroxidation in ferroptotic cell death. ACS Cent Sci 3: 232-243, 2017.
14. Kajarabille N and Latunde-Dada GO: Programmed cell-death by ferroptosis: Antioxidants as mitigators. Int J Mol Sci 20: 4968, 2019.
15. Qin B, Wang Q, Lu Y, Li C, Hu H, Zhang J, Wang Y, Zhu J, Zhu Y, Xun Y and Wang S: Losartan ameliorates calcium oxalate-induced elevation of stone-related proteins in renal tubular cells by inhibiting NADPH oxidase and oxidative stress. Oxid Med Cell Longev 2018: 1271864, 2018.
16. Hu Z, Zhang H, Yi B, Yang S, Liu J, Hu J, Wang J, Cao K and Zhang W: VDR activation attenuate cisplatin induced AKI by inhibiting ferroptosis. Cell Death Dis 11: 73, 2020.
17. Song Q, Liao W, Chen X, He Z, Li D, Li B, Liu J, Liu L, Xiong Y, Song C and Yang S: Oxalate activates autophagy to induce ferroptosis of renal tubular epithelial cells and participates in the formation of kidney stones. Oxid Med Cell Longev 2021: 6630343, 2021.
18. Chawla LS and Kimmel PL: Acute kidney injury and chronic kidney disease: An integrated clinical syndrome. Kidney Int 82: 516-524, 2012.
19. Wang F, Lv H, Zhao B, Zhou L, Wang S, Luo J, Liu J and Shang P: Iron and leukemia: New insights for future treatments. J Exp Clin Cancer Res 38: 406, 2019.
20. Masaldan S, Belaidi AA, Ayton S and Bush AI: Cellular senescence and iron dyshomeostasis in Alzheimer's disease. Pharmaceuticals (Basel) 12: 93, 2019.
21. Alvarez SW, Sviderskiy VO, Terzi EM, Papagiannakopoulos T, Moreira AL, Adams S, Sabatini DM, Birsoy K and Possemato R: NFS1 undergoes positive selection in lung tumours and protects cells from ferroptosis. Nature 551: 639-643, 2017.
22. Tang S and Xiao X: Ferroptosis and kidney diseases. Int Urol Nephrol 52: 497-503, 2020.
23. Miess H, Dankworth B, Gouw AM, Rosenfeldt M, Schmitz W, Jiang M, Saunders B, Howell M, Downward J, Felsher DW, *et al*: The glutathione redox system is essential to prevent ferroptosis caused by impaired lipid metabolism in clear cell renal cell carcinoma. Oncogene 37: 5435-5450, 2018.
24. Miotto G, Rossetto M, Di Paolo ML, Orian L, Venerando R, Roveri A, Vučković AM, Bosello Travain V, Zaccarin M, Zennaro L, *et al*: Insight into the mechanism of ferroptosis inhibition by ferrostatin-1. Redox Biol 28: 101328, 2020.
25. Skouta R, Dixon SJ, Wang J, Dunn DE, Orman M, Shimada K, Rosenberg PA, Lo DC, Weinberg JM, Linkermann A and Stockwell BR: Ferrostatins inhibit oxidative lipid damage and cell death in diverse disease models. J Am Chem Soc 136: 4551-4556, 2014.
26. Khan SR: Reactive oxygen species as the molecular modulators of calcium oxalate kidney stone formation: Evidence from clinical and experimental investigations. J Urol 189: 803-811, 2013.
27. Hu ZX, Zhang H, Yang SK, Wu XQ, He D, Cao K and Zhang W: Emerging role of ferroptosis in acute kidney injury. Oxid Med Cell Longev 2019: 8010614, 2019.
28. Wang J, Liu Y, Wang Y and Sun L: The cross-link between ferroptosis and kidney diseases. Oxid Med Cell Longev 2021: 6654887, 2021.
29. Jiang GP, Liao YJ, Huang LL, Zeng XJ and Liao XH: Effects and molecular mechanism of pachymic acid on ferroptosis in renal ischemia reperfusion injury. Mol Med Rep 23: 63, 2021.
30. Zou YL and Schreiber SL: Progress in understanding ferroptosis and challenges in its targeting for therapeutic benefit. Cell Chem Biol 27: 463-471, 2020.
31. Zhang X and Li X: Abnormal iron and lipid metabolism mediated ferroptosis in kidney diseases and its therapeutic potential. Metabolites 12: 58, 2022.
32. Wang Y, Quan F, Cao Q, Lin Y, Yue C, Bi R, Cui X, Yang H, Yang Y, Birnbaumer L, *et al*: Quercetin alleviates acute kidney injury by inhibiting ferroptosis. J Adv Res 28: 231-243, 2020.
33. Yaito Y, Fujii A, Sawada H, Oboshi M, Iwasaku T, Okuhara Y, Morisawa D, Eguchi A, Hirotani S and Masuyama T: Association between renal iron accumulation and renal interstitial fibrosis in a rat model of chronic kidney disease. Hypertens Res 38: 463-470, 2015.
34. Ikeda Y, Ozono I, Tajima S, Imao M, Horinouchi Y, Izawa-Ishizawa Y, Kihira Y, Miyamoto L, Ishizawa K, Tsuchiya K and Tamaki T: Iron chelation by deferoxamine prevents renal interstitial fibrosis in mice with unilateral ureteral obstruction. PLoS One 9: e89355, 2014.

35. Wang L, Zhang Z, Li M, Wang F, Jia Y, Zhang F, Shao J, Chen A and Zheng S: P53-dependent induction of ferroptosis is required for artemether to alleviate carbon tetrachloride-induced liver fibrosis and hepatic stellate cell activation. IUBMB Life 71: 45-56, 2019.
36. Zhang Z, Yao Z, Wang L, Ding H, Shao J, Chen A, Zhang F and Zheng S: Activation of ferritinophagy is required for the RNA-binding protein ELAVL1/HuR to regulate ferroptosis in hepatic stellate cells. Autophagy 14: 2083-2103, 2018.
37. Gong Y, Wang N, Liu N and Dong H: Lipid peroxidation and GPX4 inhibition are common causes for myofibroblast differentiation and ferroptosis. DNA Cell Biol 38: 725-733, 2019.
38. Ye Z, Xia Y, Zhou X, Li B, Yu W, Ruan Y, Li H, Ning J, Chen L, Rao T and Cheng F: CXCR4 inhibition attenuates calcium oxalate crystal deposition-induced renal fibrosis. Int Immunopharmacol 107: 108677, 2022.